Ceramics International 46 (2020) 22108–22115

Contents lists available at ScienceDirect

Ceramics International

journal homepage: www.elsevier.com/locate/ceramint

Trivalent gadolinium doped $SrZrO_3$ perovskite ceramic: Sol-gel synthesis, paramagnetic centres, and luminescence studies

N. Singh[a,1], In-Won Kim[a,1], S. Watanabe[b], T.K. Gundu Rao[b], Vijay Singh[a,*]

[a] Department of Chemical Engineering, Konkuk University, Seoul, 05029, Republic of Korea
[b] Institute of Physics, University of Sao Paulo, SP, 05508-090, Brazil

ARTICLE INFO

Keywords:
Perovskite ceramic
$SrZrO_3$
Sol-gel
EPR
Gd^{3+}
Luminescence

ABSTRACT

Trivalent gadolinium (Gd^{3+}) doped $SrZrO_3$ perovskite ceramic has been prepared and their X-ray diffraction (XRD), Fourier-transform infrared spectroscopy (FT-IR), scanning electron microscopy (SEM), electron paramagnetic resonance (EPR), and photoluminescence (PL) spectra are recorded. The existence of divalent and tetravalent cations in $SrZrO_3$ along with a trivalent dopant ion provides an opportunity to study the effect of charge compensators on the system properties. The cubic phase is evident from XRD diffraction patterns of the product. The SEM analysis suggests the formation of voids and pores in the ceramics caused by gases those liberated during the process of sintering. The EPR technique has been used to investigate the un-doped and Gd^{3+}-doped $SrZrO_3$ ceramics. The un-doped $SrZrO_3$ shows an axially symmetric EPR line with $g_{\|} = 1.94$ and $g_{\perp} = 1.99$, which is attributed to the Zr^{3+} ion. The Gd^{3+}-doped $SrZrO_3$ shows dominant EPR lines with effective g-values at 1.93, 2.04, and 2.35. Weak lines are observed at 2.72, 3.64, 6.08, and 15.5. At higher dopant concentrations, a broad line with $g_{eff} \sim 2.1$ is seen, together with low field lines. In the low field region of the EPR spectrum, lines appear because of immediate environment distortions. Under the excitation of 273 nm, the emission spectrum shows band $^6P_{7/2} \rightarrow {}^8S_{7/2}$ (313 nm). The emission at 313 nm suggests that the prepared sample can be used as a narrow band UV radiation source. Emission and EPR analysis of the sample confirm that Gd^{3+} is distributed in both Sr^{2+} and Zr^{4+} sites in the $SrZrO_3$ matrix.

1. Introduction

Lanthanide and actinide ions-doped oxide ceramics with a perovskite structure AMO_3 (A = Ca, Pb, Sr, Cd, Ba, M = Ti, Zr) are important materials because of their various physical properties, such as superconductivity, magnetic, ionic conductivity, etc. [1–5]. A perovskite structure has many applications in the field of solid oxide fuel, cells, optical coatings, gas sensors, electronic ceramics, hydrogen sensors, and filters [5–11]. Besides these applications, a perovskite structure can be used for high-level nuclear waste disposal [12].

Strontium zirconate ($SrZrO_3$) associates with the perovskite oxide family and it has a huge number of technologically important applications in the fields of solid oxide fuel, optical coatings, catalysts, gas sensors, luminescent materials, refractory materials, proton conductors, etc. [13–19]. Recently, much research has been performed on lanthanide and actinide ion-doped perovskite oxides. Sheetal [20] investigated $SrZrO_3$:Eu^{3+} phosphor optical and structure properties. Gupta et al. [21] reported visible light emitting Sm^{3+}-, Eu^{3+}-, and Dy^{3+}-doped $SrZrO_3$. Jin et al. [22] published luminescence studies of long afterglow $SrZrO_3$:Pr^{3+} phosphor. $SrZrO_3$ doped with Eu^{3+} phosphor was explored by Huang et al. [23] and Zhang et al. [24]. The synthesis and optical characterization of $SrZrO_3$:Ce nanoparticles was reported by Rétot [25]. $SrZrO_3$ perovskite compounds doped with Ce^{3+}, Ho^{3+}, Eu^{3+}, Dy^{3+}, Er^{3+}, and Yb^{3+} ions were prepared and investigated by several groups [26–30]. Recently, Gupta et al. [31] synthesized a uranium (U) ion in $SrZrO_3$ perovskite and suggested that zirconate-based perovskite materials are an apparent nominee for immobilization of nuclear wastage.

$SrZrO_3$ belongs to AMO_3 family of perovskites and has a distorted perovskite structure with the orthorhombic structure [32]. AMO_3 compounds have larger cation occupies the A-site while the smaller cations in M-sites. Sr ions are located in 8-fold coordination while Zr ions have 6-fold octahedral coordination. The crystal structure investigation on $SrZrO_3$ perovskite are already discussed and reported in the literature [32–35].

Trivalent gadolinium (Gd^{3+}) is one of the lanthanide metal ions

* Corresponding author.
E-mail address: vijayjiin2006@yahoo.com (V. Singh).
[1] These authors contributed equally to this work.

https://doi.org/10.1016/j.ceramint.2020.05.261
Received 31 March 2020; Received in revised form 13 May 2020; Accepted 25 May 2020
Available online 30 May 2020

Table 1
Detailed information of sample composition and starting materials.

Sample composition	Starting materials			
$SrZrO_3$:0.01Gd	Sr = 0.8464 g	Zr = 1.0688 g	C.A = 3.0738 g	Gd = 0.0180 g
$SrZrO_3$:0.03Gd	Sr = 0.8464 g	Zr = 1.0688 g	C.A = 3.0738 g	Gd = 0.0541 g
$SrZrO_3$:0.05Gd	Sr = 0.8464 g	Zr = 1.0688 g	C.A = 3.0738 g	Gd = 0.0902 g
$SrZrO_3$:0.07Gd	Sr = 0.8464 g	Zr = 1.0688 g	C.A = 3.0738 g	Gd = 0.1263 g
$SrZrO_3$:0.09Gd	Sr = 0.8464 g	Zr = 1.0688 g	C.A = 3.0738 g	Gd = 0.1624 g
$SrZrO_3$:0.11Gd	Sr = 0.8464 g	Zr = 1.0688 g	C.A = 3.0738 g	Gd = 0.1985g

Sr = $Sr(NO_3)_2$, Zr = $ZrO(NO_3)_2{\cdot}2H_2O$, C.A = $C_6H_8O_7$, Gd = $Gd(NO_3)_3{\cdot}6H_2O$.

with a $4f^7$ electronic configuration where all the seven unpaired electrons contribute to its high electron spin. The Gd^{3+} ions in several hosts have been investigated because of their UV radiation–emitting properties [36]. Ultraviolet radiation has been extensively used in several applications, such as photolithography, UV curing, polymerization, and chemical reactions [37–40]. Furthermore, UV light is useful in sterilization, treatment of incurable skin diseases, and generation of vitamins D_2 and D_3 [41–43]. It appears that Gd^{3+} in particular is a suitable activator ion. The levels $^6P_{7/2}$ to $^8S_{7/2}$ of the transition can give a narrow band of emissions at around 312–315 nm, which is suitable for treating many kinds of skin diseases [44,45]. In recent years, Gd^{3+} has been found suitable for the preparation of computed tomography contrast agents. It has been noticed that for radiosensitization enhancement, Gd^{3+} is the most widely employed lanthanide element. Further, Gd^{3+} ion has interesting optical and electron paramagnetic resonance (EPR)/electron spin resonance (ESR) spectroscopic properties. EPR/ESR spectroscopy technique has high sensitivity and can substantiate the data obtained from optical spectroscopy. Accordingly, Gd^{3+} can also be used as a probe to acquire information about the local environment in any given host lattice. Keeping in view of the great demand of UV emitting phosphors and to probe the local environment, the present work was undertaken. Furthermore, a cursory glance at the literature reports suggests that the EPR spectrum of Gd^{3+} ions in distorted perovskite structure is poorly understood. In this context, we have prepared Gd^{3+} doped perovskite by sol-gel process and investigated the spectroscopic properties using EPR technique and tried to correlate the data with observed optical properties. Further, EPR is very sensitive for the paramagnetic ions in both the magnetic and nonmagnetic substances. EPR also gives details of local environment, site-occupation, structural symmetry, and oxygen vacancies adjacent to paramagnetic ions. Due to the $4f^7$ electronic configuration ($^8S_{7/2}$), Gd^{3+} ion EPR signals can be observed even at room temperature. The understanding of the Gd^{3+} ions site symmetries in a $SrZrO_3$ perovskite ceramic would be of better support, and EPR could provide this knowledge. $SrZrO_3$ lattice contains divalent Sr^{2+} and tetravalent Zr^{4+} ions. This could lead different kind of charge compensators when a trivalent dopant ion like Gd^{3+} ion is present in the lattice. These charge compensators have the possibility of inducing distortions in their immediate surroundings. These distortions could get reflected in the EPR spectrum of the dopant ion.

The sol-gel procedure is accepted as one of the important methods for synthesizing various ceramic powders [46–48]. It has several advantages over conventional solid-state methods, such as better homogeneity, easier control of composition, and low processing temperatures. Taking this point into consideration, we prepared $SrZrO_3$:xGd ($x = 0.01 \leq x \leq 0.11$) using the sol-gel technique, and X-ray diffraction (XRD), scanning electron microscope (SEM), Fourier transform infrared (FTIR), EPR and photoluminescence techniques were used to characterize the prepared samples. Investigations of the correlation between EPR and optical studies of synthesized Gd-doped $SrZrO_3$ perovskite ceramics are very important in efforts to design $SrZrO_3$ perovskite ceramic-based material, as well as exploring it for other lanthanides.

2. Experimental

$SrZrO_3$:xGd ($x = 0.01 \leq x \leq 0.11$) ceramic is synthesized through sol-gel procedure. For the preparation of samples, strontium nitrate ($Sr[NO_3]_2$) (Sigma Aldrich, purity: 99%), zirconium nitrate oxide dihydrate ($ZrO[NO_3]_2{\cdot}2H_2O$) (Kanto chemical, purity: 99%), gadolinium nitrate hexahydrate ($Gd[NO_3]_3{\cdot}6H_2O$) (Sigma Aldrich, purity: 99.9%) and citric acid ($C_6H_8O_7$) (Junsei, purity: 99.5%) are used as received without any further purification. The sol-gel synthesis involves dissolution of metal nitrates ion precursors in a suitable solvent and obtaining gel by addition of a chelating agent (citric acid). Usually, a certain ratio of metal nitrate and citric acid is used to get respective metal oxides. In this investigation the citric acid to total metal ion ratio is 2:1. Configuration of the samples and initial substances are described in Table 1. First, all starting compounds are measured in a beaker (100 ml) and liquified with a 10 ml of de-ionized water over a stirrer. The milky sol is collected after 1 h of stirring. Then the sol is stored in an oven of 110 °C temperature till it formed dried xerogels. Afterward, the brown gel is transferred into a china dish and calcinated in a 400 °C hot furnace up to 2 h. Later, the preheated black residuals powder is finely crushed and post heated at 1050 °C for 4hr in air. The endmost powders are used for the characterization.

The phase formation investigation of the powders is checked by powder X-ray diffraction (XRD) analysis with a RIGAKU Miniflex-II diffractometer. CuKα radiation (λ = 1.5406 Å) is used as an X-ray source. The diffractometer is operated at 40 kV and 30 mA. The patterns of XRD are carried out on a fixed scan rate of 5°/minute using the range 10 to 80° of 2θ. A S-3400 (Hitachi, Japan) SEM is utilized for the morphology investigation. The vibrational modes of the prepared ceramic are checked by Rx1 instrument (PerkinElmer) in the range of 400–4000 cm^{-1}. The photoluminescence excitation and photoluminescence studies are conducted by employing a RF-5301PC (SHIMADZU), spectrofluorophotometer (Xenon lamp equipped). By operating an ESR (JEOL FE1X) spectrometer of 100 kHz field modulation in X-band frequencies, the EPR spectra are collected.

3. Results and discussion

3.1. X-ray diffraction studies

The XRD patterns of un-doped $SrZrO_3$ and $SrZrO_3$:xGd ($x = 0.01 \leq x \leq 0.11$) ceramic synthesized by the sol-gel method are shown in Fig. 1. All the samples crystallized in the cubic symmetry in the space group of Pm3m. The diffraction peaks observed in the samples of $SrZrO_3$:xGd ($x = 0.01 \leq x \leq 0.11$) matched well with the powder diffraction standards references (JCPDS Card No. 76–0167), confirming the single cubic phase of $SrZrO_3$. These peaks can be indexed as (100), (110), (111), (200), (210), (211), (220), (300), (310), and (311) diffractions. From the diffraction pattern, it is observed that the host structure is not significantly altered by the incorporation of Gd^{3+} ion. Due to the fact that Gd^{3+} (1.05 Å) and Sr^{2+} (1.18 Å) have somewhat similar ionic radii, it is assumed that Gd^{3+} ions can replace Sr^{2+} ions. The FWHM (full width at half maximum) of the energetic diffraction peak was considered for the calculation of the crystallite size

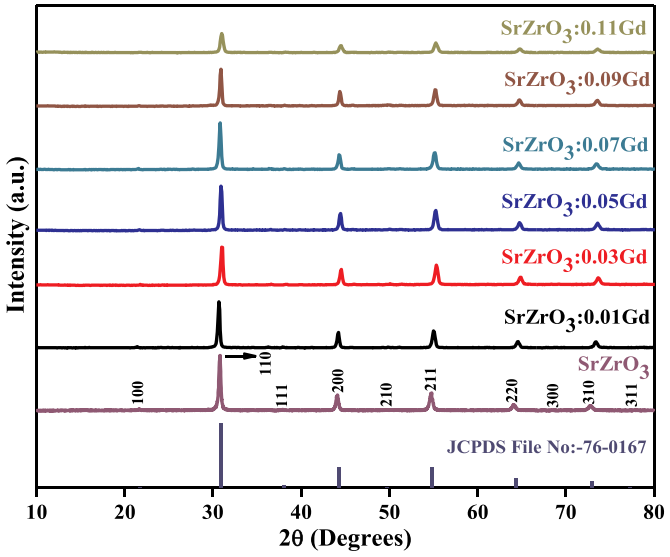

Fig. 1. XRD patterns of $SrZrO_3$:xGd (x = 0.01 ≤ x ≤ 0.11) ceramics.

Table 2
Full width at half maximum (FWHM) and crystallite size of the $SrZrO_3$:xGd (x = 0.01 ≤ x ≤ 0.11) ceramics.

Sample composition	FWHM (°)	Crystalline size (nm)
$SrZrO_3$:0.01Gd	0.2677	32.13
$SrZrO_3$:0.03Gd	0.3085	27.90
$SrZrO_3$:0.05Gd	0.2790	30.85
$SrZrO_3$:0.07Gd	0.2854	30.15
$SrZrO_3$:0.09Gd	0.2666	32.28
$SrZrO_3$:0.11Gd	0.3891	22.12

using the Scherrer's expression, $D = 0.9\lambda/\beta\cos\theta$, where, the incident X-ray wavelength is λ with θ as the Bragg's diffraction angle, and β called the FWHM of (110) peak. The crystallite size was estimated to be in the approximate 22.12–32.28 nm range and is listed in Table 2 along with FWHM for all the samples.

3.2. Scanning electron microscope studies

To investigate the surface morphology of the synthesized powder, scanning electron microscopy studies were carried out. Fig. 2 shows the SEM images of $SrZrO_3$:0.09Gd ceramic. The sample synthesized through the sol-gel mechanism are homogeneous aggregates, dense, small, irregularly shaped and distributed over the surface (see Fig. 2a and b). The irregular shape and size of the sample's particles can be associated with the non-uniform distribution of temperature during the sintering process. From Fig. 2 (c, d), it was observed that particles are highly interconnected, and the images clearly reveal both larger and smaller particles. The particles also contain voids and pores, which is most likely because of the release of a great amount of gas at the time of sintering procedure.

3.3. FT-IR studies

Fig. 3 depicts a $SrZrO_3$:0.09Gd typical FT-IR spectrum of the ceramic, in range of 400–4000 cm^{-1}. In the spectrum a strong band is displayed at around 541 cm^{-1} that correlates to Zr–O stretching vibration. Zhang et al. [49] reported the band at around 569 cm^{-1} for the $SrZrO_3$ crystals prepared by a facile hydrothermal process. The observed bands at 1431 cm^{-1} and 1463 cm^{-1} can be related to the stretching vibrations of the nitrate ion $(NO_3)^-$ [50]. The spectrum does not show a broad O–H band at around 3400 cm^{-1}, which indicates that the sample is free from water.

3.4. Electron paramagnetic resonance studies

An EPR spectrum collected at room temperature of un-doped $SrZrO_3$ is given in Fig. 4. A sharp line is noticed in free-electron region along with a low-intensity line (at g ~ 4.2). The lower field line may be ascribed to a Fe^{3+} ion present in the starting compounds used to prepare the ceramic. The defect center correlated to the line seen in the free-electron region is identified from the axially symmetric *g*-tensor with principal values $g_\perp = 1.94$ and $g_\perp = 1.99$. The center does not display any hyperfine structure. In a study of commercially available samples of ZrO_2 at room temperature, Wright and Barklie [51] report the observation of a defect center attributable to Zr^{3+} center. The center is described by an axially symmetric spectrum with principal values $g_\parallel = 1.961$ and $g_\perp = 1.976$. A number of studies have reported the observation of Zr^{3+} center which include pure zirconia powder [52], yttria stabilized zirconia [53], $Y_3Al_5O_{12}$ single crystal [54], nuclear glasses [55], YAG with Zr doping [56], Zr doped $ScPO_4$ and YPO_4 [57], polycrystalline ZrF_4 [58] and microporous Zr- silicates [59]. These systems accommodate the Zr ion in sites with low symmetry and with high co-ordination numbers such as six-fold coordinated site, seven-fold and eight-fold coordinated sites. The observed *g*-values (<2) in these systems are expected from a d^1 ion and $g_\parallel < g_\perp$ can be observed if the ion is situated in a distorted octahedral site [60]. Based on crystal field theory it has been suggested that $g_\perp \sim g_e$ and $(g_\parallel - g_e) \sim -\lambda/\Delta$ [61]. Here, λ is the constant of spin-orbit coupling (λ ~ 500 cm^{-1} in case of Zr^{3+} ion) and the splitting across the E (cubic crystal field) and T_2 levels is Δ.

$SrZrO_3$ is one of the many compounds which belong to the AMO_3 family of perovskites. These compounds have a large cation at A-site while a smaller ion occupies the M-site. Oxygen ions serve as a bridging ligand connecting M-site cations to form a 3-d cage-like framework. The basic blocks which build the structure are Sr ions which have eight-fold coordination and Zr ions with six-fold coordination [SrO_8 and ZrO_6] [62]. In $SrZrO_3$, there are divalent Sr^{2+} ions and tetravalent Zr^{4+} ions. As tetravalent ions are present in the lattice, there will be a partial replacement of Sr^{2+} ions with Zr^{4+} ions because of antisite cation disorder. In crystals, an antisite cation exchange or disorder is a point defect. Theoretical estimations anticipate such disorders can exist in a crystal lattice [63]. The fine structure of X-ray absorption and the diffraction studies have confirmed the presence of such defects [64,65] and they are also directly observed by advanced scanning electron microscopy [66]. Because of cation disorder and non-stoichiometry, oxygen vacancies may form in the lattice. It may be cited that theoretical estimations advise the ease of oxygen vacancy formation in lattices with cation exchange disorder in comparison with a lattice without any such disorder [67].

On the basis of the previous conclusions mentioned earlier, center I showing an axial spectrum (Fig. 4) and *g*-values less than the value of free-electron in $SrZrO_3$ is tentatively analyzed as a Zr^{3+} center. A Zr^{3+} ion occupying a site which deviates from octahedral symmetry displays an axial *g*-tensor. In the perovskite AMO_3 structure, A ions occupy holes which are situated between the MO_6 octahedra. The radius of M ion determines hole size for A ion. In the particular case of M ion being Zr^{4+}, the hole radius of is 0.160 nm [62] as determined from the ionic radii given by Shannon and Prewitt [68]. In twelve-fold coordinated sites, the Ba^{2+} ion radius is 0.160 nm. In the case of $BaZrO_3$, the cubic perovskite displays practically no distortion. Here, in 12-fold co-ordinated sites, the radius of Ba^{2+} ion is 0.160 nm. On the other hand, in $SrZrO_3$, the Sr^{2+} ion has a smaller ionic radius (0.144 nm) than the undistorted structure's hole (0.160 nm). The presence of a small ion causes lowering of symmetry as compared to the perovskite structure of ideal case. Further, there will be distortions of ZrO_6 octahedra caused

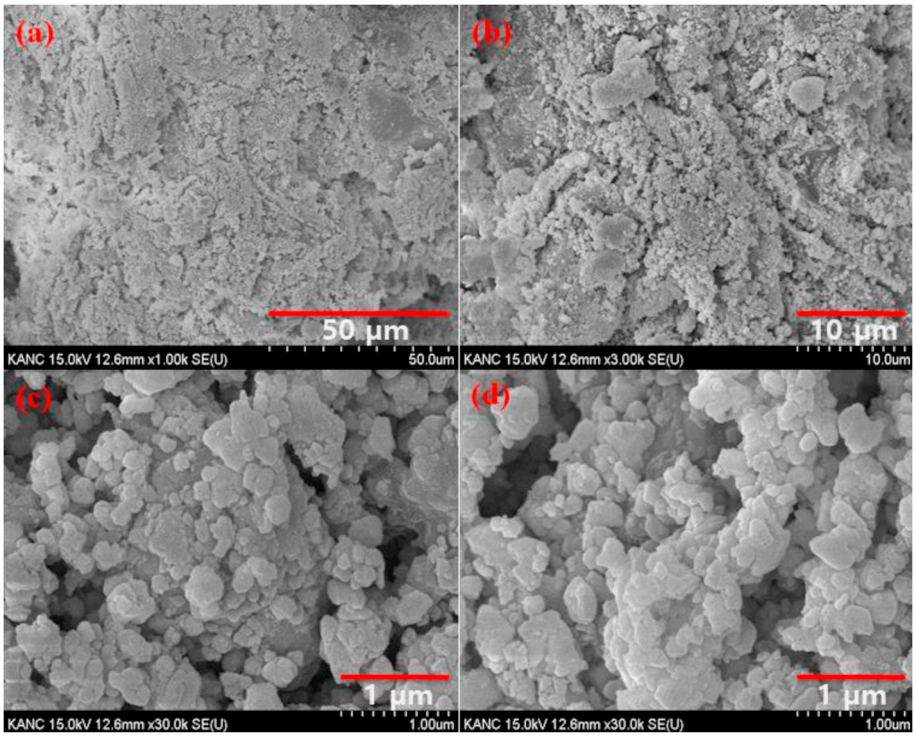

Fig. 2. SEM images of $SrZrO_3$:0.09Gd ceramic.

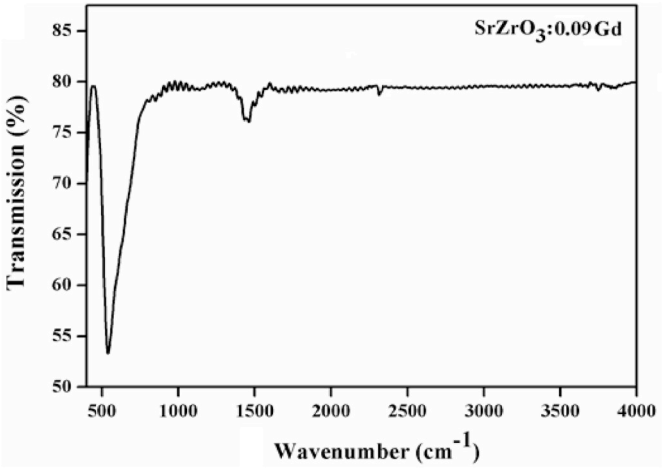

Fig. 3. FT-IR spectrum of $SrZrO_3$:0.09Gd ceramic.

by the presence of oxygen vacancies in lattice because of the antisite disorder. These vacancies cause oxygen rearrangements which are closer to ion of Zr^{4+}. Distortions ensuing from these causes result in *g*-tensor of the Zr^{3+} ion being axial in nature.

Fig. 4 illustrates the room temperature EPR spectrum of Gd^{3+} doped $SrZrO_3$ ceramics. This spectrum is dominated by relatively high-intensity lines with effective g-values at g_{eff} ~1.93, 2.04, 2.35 and 2.72. There are low-intensity lines at g_{eff} ~3.64, 6.08 and 15.5. Usually, a simple spectrum is observed with main EPR line near g ~2.0023 for S-state ions Gd^{3+} and Eu^{2+}. This spectrum results from experiencing a weak crystal field by the ion located at relatively undistorted sites in the lattice. In cases where the surroundings are distorted as it is in zeolites and glasses, the spectrum looks different with three EPR lines observed at an effective g_{eff} of 2.0, 2.8 and 5.9. This kind of spectrum is called as a U-spectrum and is typical in distorted systems of the Gd^{3+} ions. When concentration of dopant Gd^{3+} ion is increasing, a wide line appears (line width ~ 1130 G) superimposed on the distinct narrow lines. The corresponding EPR spectrum with increasing the concentration of dopant is displayed in Fig. 4.

Apart from disordered systems like glasses and zeolites, there are examples where a spectrum of U-spectrum kind has been noticed [69]. The origin of U-spectrum lies in the crystal field which varies from one Gd^{3+} site to the other. Essentially, a distribution of crystal field is created by distortions varying from one site to the other.

The type of EPR spectrum that can be observed under different conditions and also the discussion of U-spectrum has been reported by Brodbeck and Iton [70]. According to them, lines near to g ~2.0 region are expected for the case of an ion facing a weak crystal field and located in a relatively undistorted environment. In distorted surroundings, the ion of Gd^{3+} experiences stronger crystal field (intermediate crystal field according to Brodbeck and Iton notation) and now lines in the low field region will occur.

In an eight-fold coordination Sr^{2+} ion has an ionic radius of 1.26 Å [71]. The ionic radius of Zr^{4+} ion in a 6-fold coordination is 0.72 Å. Besides, Gd^{3+} ion has an ionic radius of 0.938 Å in 6-fold and 1.05 Å in 8-fold coordination. Zhang et al. [49] have studied $SrZrO_3$ doped with the Yb^{3+} ion. Sr^{2+} ion (ionic radius: 1.26 Å) has a lager ionic radius than the ionic radius of Yb^{3+} ion (0.87 Å). On the other hand, the ionic radius of Yb^{3+} is larger than the ionic radius of Zr^{4+} ion (0.72 Å). On doping with Yb^{3+}, if Yb^{3+} is located at Sr^{2+} sites, then the unit cell constant would show a decreased value. If ion of Yb^{3+} occupies sites of Zr^{4+}, then there would be increment in the unit cell constant. Zhang et al. [49] observed that the values of lattice constant are lower in the doped sample than in an un-doped sample. This led them to conclude that Yb^{3+} ion most likely occupies Sr^{2+} sites in $SrZrO_3$. In the present case, the ionic radius of the Gd^{3+} ion is smaller than the Sr^{2+} ion radius. Therefore, on the basis of observations of Zhang et al. [49], there is a strong possibility that Gd^{3+} ion is located at Sr^{2+} sites in $SrZrO_3$. In this context, it may be mentioned that in a study of Eu^{3+} doped $SrZrO_3$ ceramic, PL results of Huang et al. [23] showed that Eu^{3+} ion occupies

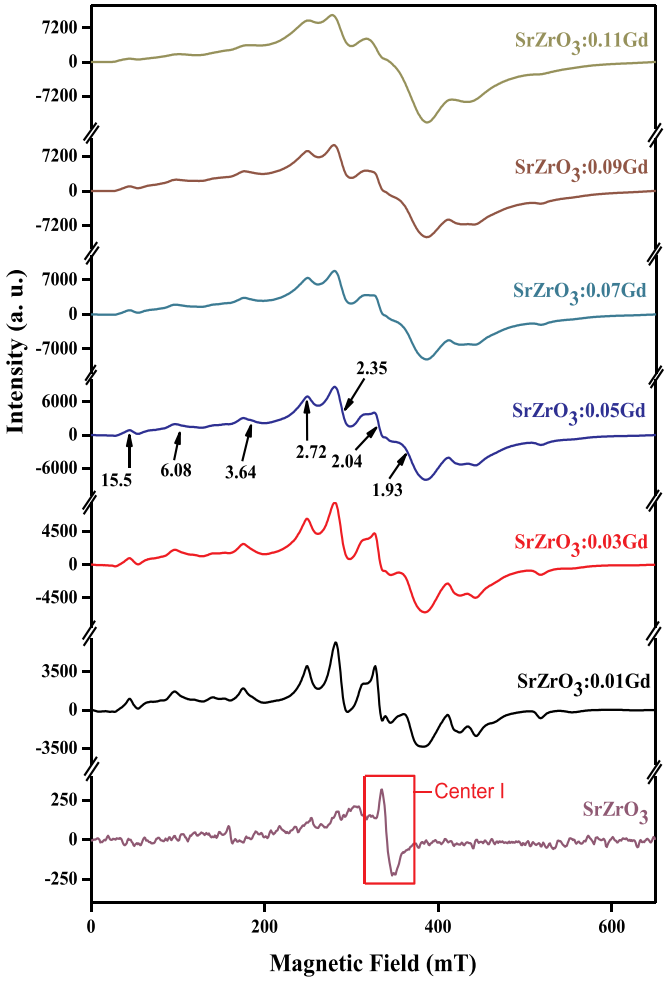

Fig. 4. EPR spectra of pure $SrZrO_3$ and $SrZrO_3$:xGd ($x = 0.01 \leq x \leq 0.11$) ceramics. Center I seen in pure $SrZrO_3$ is due to Zr^{3+} ion.

two sites in $SrZrO_3$ viz., Sr^{2+} and Zr^{4+}. As the ionic radius difference between Sr^{2+} and Eu^{3+} is the same as Eu^{3+} and Zr^{4+}, Eu^{3+} ion may occupy either Zr^{4+} sites or Sr^{2+} sites. In another study on $SrZrO_3$:Eu^{3+} phosphor, Gupta et al. [21] inferred on the basis of time-resolved emission data that Eu^{3+} ion is located at more than one site in the phosphor. Thus, a possibility is there that Gd^{3+} ion may be located at Sr^{2+} as well as at Zr^{4+} sites in $SrZrO_3$.

In a study of the effects of doping rare-earth (RE) ions (Gd^{3+} and Sm^{3+}) on the thermo-physical properties of $LaMgAl_{11}O_{19}$ (LMA) phosphor, Jiansheng and Yanli [72] have concluded based on XRD results that the RE ions substitute La^{3+} sites in LMA. They further observed chemical bonds strengthening and also shortening of bonds with increased RE ion concentration in the lattice. These observations resulted from their Raman investigations of LMA system. They conclude that the presence of Gd^{3+} ions with smaller ionic radius at the sites of La^{3+} ion which has higher ionic radius results in distortions of the LaO_2 network leading to local distortions. If there are distortions in the immediate neighborhood of Gd^{3+} ion, then the crystal field observed by the ion will increase. According to Brodbeck and Iton [70], in the lower field region of the spectrum, EPR lines will now appear. In $SrZrO_3$, Gd^{3+} ion with smaller ionic radius substitutes Sr^{2+} with higher ionic radius, a situation similar to Gd^{3+} ion LMA system. Therefore, in lower field region distinct lines are expected which is in agreement with EPR spectrum observed in low dopant concentration $SrZrO_3$:Gd ceramic. Fig. 4 shows the changes in the EPR spectrum with increasing dopant concentration. A wide line (line width about 1130 G) and an approximate *g*-value of 1.945 appear and increase in intensity with Gd ion concentration. The broad line is speculated to be due to Gd^{3+} ion situated at the Zr^{4+} site in the $SrZrO_3$ ceramic. Broad EPR line suggests that the Gd^{3+} ions in the second Zr^{4+} sites are close to one another which results in dipolar interaction across the ions. It is observed that the intensity of Gd^{3+} lines at Sr^{2+} sites (distinct low field lines) do not change with increase of dopant Gd^{3+} concentration. On the other hand, the broad line most likely coming from Gd^{3+} ions at Zr^{4+} sites increase in intensity with increasing dopant concentration. This suggests that at higher concentrations, Gd^{3+} ion prefers Zr^{4+} sites and there is selective occupation of cation sites in $SrZrO_3$ lattice.

3.5. Photoluminescence studies

Fig. 5 displays the emission and excitation spectra of the $SrZrO_3$:xGd ($x = 0.01 \leq x \leq 0.11$) ceramic. Fig. 5a shows the photoluminescence excitation spectra of samples obtained by monitoring the strongest emission at 313 nm of the Gd^{3+} ion. The excitation spectra are a bunch of several narrow bands and a weak broad band. The weak wide band centered at about 228 nm may be because of the host lattice absorption. Huang et al. [23] observed a very sharp and intense peak at 229 nm, which they attributed to transfer of charge from the oxygen ligands to the central zirconium atom within the ZrO_3^{2-} group. It was observed that the set of bands in 240–290 nm range corresponded to the characteristic Gd^{3+} transitions from the ground state of $^8S_{7/2}$ to the excited states of ^6D_J and ^6I_J. The bands at 244, 246, 252, 273, 275, and 278 nm can be ascribed to the $^8S_{7/2} \rightarrow {}^6D_{5/2,\ 3/2}$, $^8S_{7/2} \rightarrow {}^6D_{7/2}$, $^8S_{7/2} \rightarrow {}^6D_{9/2}$, $^8S_{7/2} \rightarrow {}^6I_{15/2,\ 13/2}$, $^8S_{7/2} \rightarrow {}^6I_{9/2}$, $^6I_{17/2}$, and $^8S_{7/2} \rightarrow {}^6I_{7/2}$ transitions of the Gd^{3+}, respectively [69,70]. The noticed band agree well with the previous observations [32,73,74]. Fig. 5b describes the fitted excitation spectra with six Gaussian peaks and the fitted data. The intensity of the band at 273 nm is found to be maximum compared to other bands; therefore, it was chosen for collecting the emission spectra of the ceramic.

The emission spectra of various Gd^{3+} ion concentrations in $SrZrO_3$ are recorded in the 305–325 nm range with the excitation at 273 nm (Fig. 5 (c)). The emission spectra show several bands at 307, 313, 316, and 321 nm. The emission band at 307 nm can be associated to $^6P_{5/2} \rightarrow {}^8S_{7/2}$ transitions of the Gd^{3+} ion. The emission bands at 313, 316, and 321 nm can be associated to the $^6P_{7/2} \rightarrow {}^8S_{7/2}$ transitions of the Gd^{3+} ion. The emission spectra reveal that the intensity of 313 nm and 316 nm bands varies by increasing the concentrations of Gd^{3+}. As the Gd^{3+} concentration increases, the intensity of the 316 nm band increases more than the 313 nm band (Fig. 6a). Therefore, Gd^{3+} ion is possibly situated at the Sr^{2+} and Zr^{4+} sites in $SrZrO_3$ ceramic. The FWHM of the emission band at 313 and 316 nm does not show the systematic trend as the Gd^{3+} ion concentration increases (Fig. 6b). Interestingly, in a manner similar to the FWHM of the X-ray diffraction peaks, the FWHM of the emission bands at 313 and 316 nm did not display a systematic trend. The emission intensity of 313 nm and 316 nm bands increases as the Gd^{3+} increased up to 0.09 mol, and thereafter the intensity decreases (Fig. 6a). This can be associated to the result of common concentration quenching mechanism. The PL spectra reveal that the optimum Gd^{3+}-doped contents of $SrZrO_3$:xGd ($x = 0.01 \leq x \leq 0.11$) ceramic is 0.09 mol. In many cases, the concentration quenching mechanism of RE ions is generally because of transfer of the non-radiative energy process in between RE ions. The concentration quenching may take place via exchange interaction or electric multipolar interaction. The R_c (critical distance) for non-radiative energy transfer can be used to calculate the correct mechanism responsible for concentration quenching. The R_c of energy transfer estimated by the following formula:

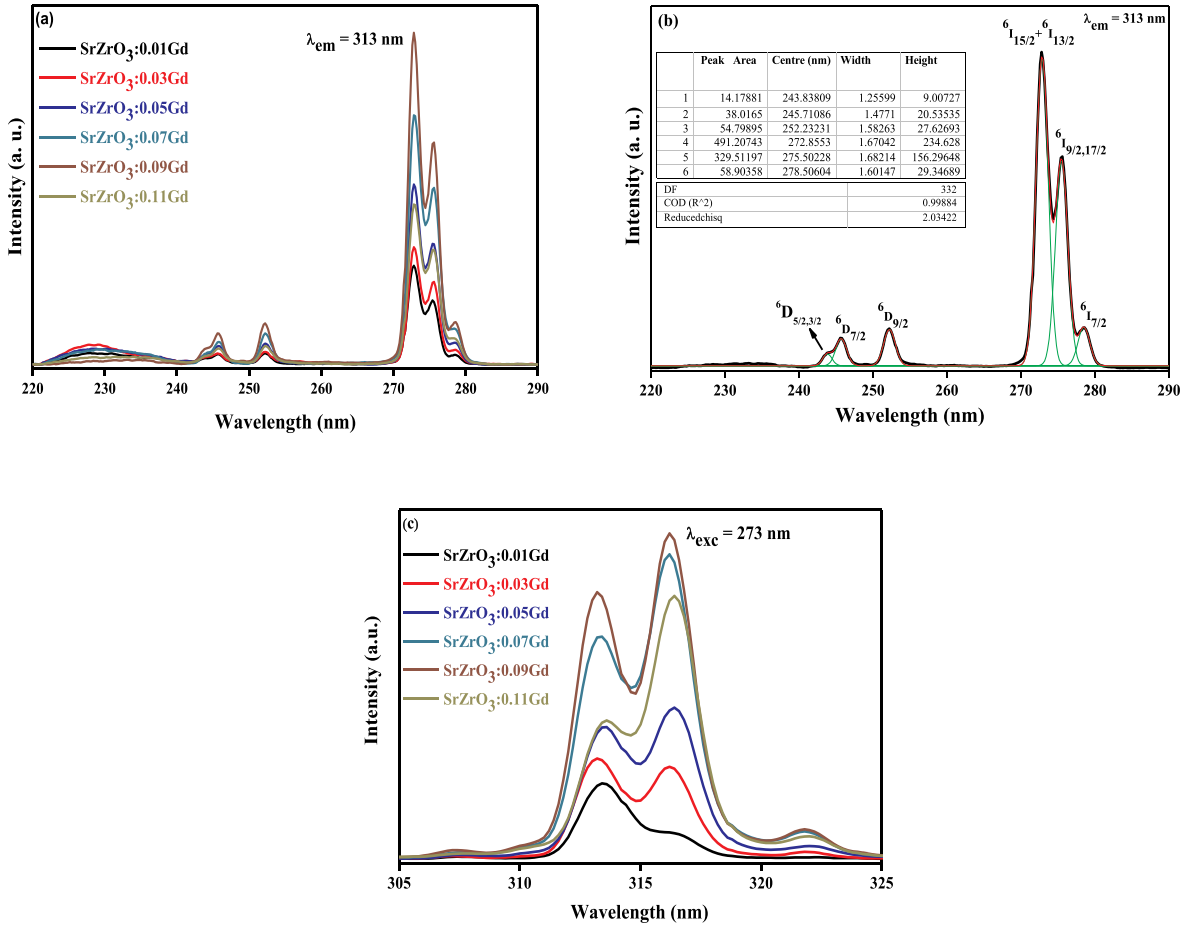

Fig. 5. (a) Excitation spectra of $SrZrO_3$:xGd (x = 0.01 ≤ x ≤ 0.11) ceramics (λ_{em} = 313 nm), (b) Fitted excitation spectrum with seven Gaussian peaks along with fitted data, and (c) emission spectra of $SrZrO_3$:xGd (x = 0.01 ≤ x ≤ 0.11) ceramics (λ_{exc} = 273 nm).

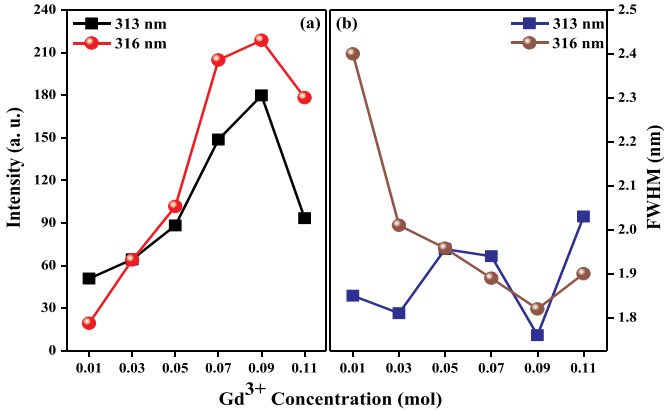

Fig. 6. (a) Variation of emission intensity ($I_{313\ nm,\ 316\ nm}$), and (b) FWHM of 313 nm and 316 nm emission band as a function of Gd^{3+} concentration.

$$R_c \approx 2[\frac{3V}{4\pi\chi_c N}]^{1/3}$$

where, V indicates volume of unit cell of $SrZrO_3$ (552.175 $(Å)^3$) [75], χ_c denotes Gd^{3+} critical concentration at the occurrence of concentration quenching (0.09) and in unit cell (4) the number of Z ions are denoted by N. For non-radiative energy transfer the calculated critical distance was 14.30 Å. The value of critical distance R_c express that there has no occurrence of energy transfer, because of the exchange interaction, but the energy transferred among the nearest-neighbor ions is due to the multipolar interaction. Fig. 7 depicts the energy level layout for the Gd^{3+} ion. From this figure, it can be seen that Gd^{3+} ions are excited from ^8S state to ^6I state. Afterward, ions relax to the level of the ^6P state by the process of non-radiative energy transfer. Finally, the ions from ^6P state relax to the ^8S state of Gd^{3+} and give the UVB emission.

4. Conclusions

Varied concentrations of Gd^{3+}-doped $SrZrO_3$ perovskite ceramic is synthesized through the sol-gel procedure using citric acid. The phase purity of the un-doped and doped $SrZrO_3$ is justified by X-ray diffraction, which shows pure cubic phase products with perovskite structure. SEM images of the obtained ceramic clearly show the presence of porous formations because of gases liberated in the course of sample synthesis. The FTIR spectrum exhibited the broad band located at around 541 cm^{-1} attributed to Zr–O stretching vibration. The presence of the smaller ionic radius Gd^{3+} ion induces lattice distortions in the immediate vicinity of Gd^{3+} ion. The larger crystal field resulting from these distortions makes EPR spectrum lines appear in low field region. Emission spectroscopic studies displayed a UV radiation emission at around 313/316 nm which is associated to gadolinium stabilization in the trivalent oxidation state in $SrZrO_3$ ceramic. Based on PL and EPR data, the doped Gd^{3+} ions prefer to occupy Sr^{2+} as well as Zr^{4+} crystallographic sites in $SrZrO_3$ ceramic. This study determined that the optimum concentration of the Gd^{3+} ions, which will provide the greatest optical output, will be 0.09 mol. The PL results of the

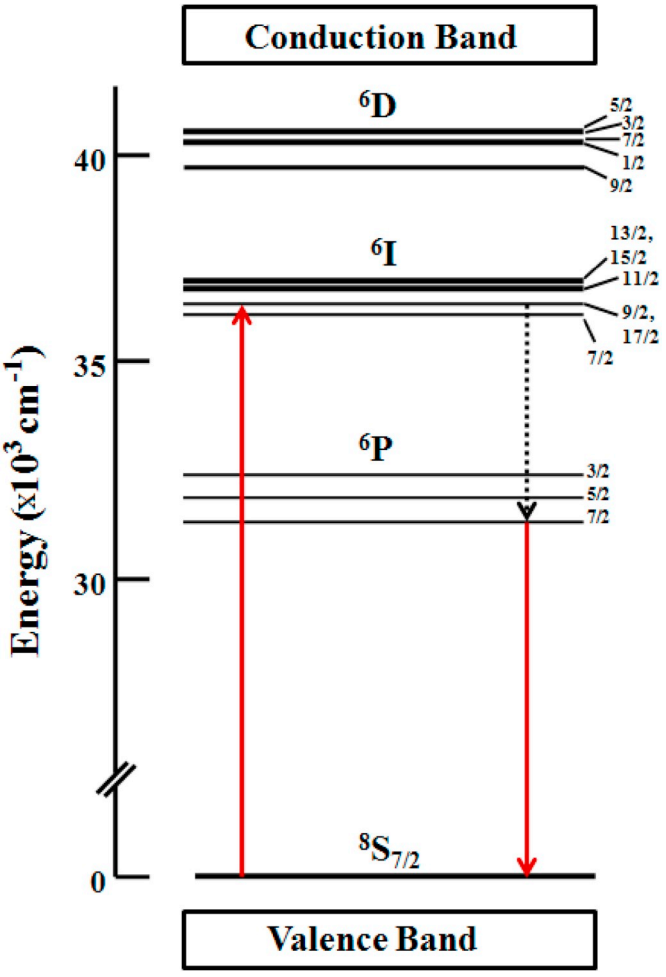

Fig. 7. The energy level diagram of Gd^{3+} ions.

synthesized Gd^{3+}-doped $SrZrO_3$ ceramic indicate that prepared sample may be utilized for the production of UVB radiation in UV fluorescent lamps.

Declaration of competing interest

The authors declare that they have no known competing financial interests or personal relationships that could have appeared to influence the work reported in this paper.

Acknowledgements

This work was supported by Konkuk University in 2016.

References

[1] M. Mohapatra, V. Natarajan, Speciation of uranium in solids using time resolved photoluminescence technique, J. Radioanal. Nucl. Chem. 302 (2014) 1327–1332.
[2] R.I. Eglitis, Ab initio hybrid DFT calculations of $BaTiO_3$, $PbTiO_3$, $SrZrO_3$ and $PbZrO_3$ (111) surfaces, Appl. Surf. Sci. 358 (2015) 556–562.
[3] K.S. Knight, C.L. Bull, Low temperature and high pressure thermoelastic and crystallographic properties of $SrZrO_3$ perovskite in the Pbnm phase, Solid State Sci. 62 (2016) 90–104.
[4] X. Wu, Y. Jiao, O. Hai, Q. Ren, F. Lin, H. Li, Effect of single and composite fluxes on the morphology and luminescence properties of layered perovskite $Sr_{1.95}TiO_4$:0.05Sm^{3+} phosphor, J. Lumin. 192 (2017) 626–633.
[5] D.K. Singh, K. Mondal, J. Manam, Improved photoluminescence, thermal stability and temperature sensing performances of K^+ incorporated perovskite $BaTiO_3$:Eu^{3+} red emitting phosphors, Ceram. Int. 43 (2017) 13602–13611.
[6] N. Bonanos, K.S. Knight, B. Ellis, Perovskite solid electrolytes: structure, transport properties and fuel cell applications, Solid State Ionics 79 (1995) 161–170.
[7] K.D. Kreuer, On the development of proton conducting materials for technological applications, Solid State Ionics 97 (1997) 1–15.
[8] A.S. Bhalla, R. Guo, R. Roy, The perovskite structure-a review of its role in ceramic science and technology, Mater. Res. Innovat. 4 (2000) 3–26.
[9] J. Cerdà, J. Arbiol, G. Dezanneau, R. Díaz, J.R. Morante, Perovskite-type $BaSnO_3$ powders for high temperature gas sensor applications, Sensor. Actuator. B Chem. 84 (2002) 21–25.
[10] Z. Cheng, J. Lin, Layered organic–inorganic hybrid perovskites: structure, optical properties, film preparation, patterning and templating engineering, CrystEngComm 12 (2010) 2646–2662.
[11] I.M. Reaney, D. Iddles, Microwave dielectric ceramics for resonators and filters in mobile phone networks, J. Am. Ceram. Soc. 89 (2006) 2063–2072.
[12] R.C. Swing, W.J. Weber, F.W. Clinard Jr., Radiation effects in nuclear waste forms for high-level radioactive waste, Prog. Nucl. Energy 29 (1995) 63–127.
[13] K. Hilpert, D. Das, M. Miller, D.H. Peck, R. Weiß, Chromium vapor species over solid oxide fuel cell interconnect materials and their potential for degradation processes, J. Electrochem. Soc. 143 (2016) 3642–3647.
[14] Q. Tian, L. Zhang, J. Liu, N. Li, Q. Ma, J. Zhou, Y. Sun, Synthesis of MoS_2/$SrZrO_3$ heterostructures and their photocatalytic H_2 evolution under UV irradiation, RSC Adv. 5 (2015) 734–739.
[15] H.-Q. Ling, A.-D. Li, D. Wu, Y.-F. Tang, Z.-G. Liu, N.-B. Ming, Fabrication and characterization of SrZrO3 thin films prepared by sol–gel, Mater. Chem. Phys. 75 (2002) 170–173.
[16] S.K. Gupta, P.S. Ghosh, N. Pathak, A. Arya, V. Natrajan, Understanding the local environment of Sm^{3+} in doped $SrZrO_3$ and energy transfer mechanism using time-resolved luminescence: a combined theoretical and experimental approach, RSC Adv. 4 (2014) 29202–29215.
[17] J.R. de Oliveira Lima, Y.A. Ghani, R.B. da silva, F.M.C. Batista, R.A. Bini, L.C. Varanda, J.E. de Oliveira, Strontium zirconate heterogeneous catalyst for biodiesel production: synthesis, characterization and catalytic activity evaluation, Appl. Catal. A-Gen. 445–446 (2012) 76–82.
[18] R. Watanabe, Y. Saito, C. Fukuhara, Dehydrogenation of ethylbenzene over zirconium-based perovskite-type catalysts of $AZrO_3$ (A: Ca, Sr, Ba), Appl. Catal. A-Gen. 482 (2014) 344–351.
[19] T. Hibino, K. Mizutani, T. Yajima, H. Iwahara, Evaluation of proton conductivity in $SrCeO_3$, $BaCeO_3$, $CaZrO_3$ and $SrZrO_3$ by temperature programmed desorption method, Solid State Ionics 57 (1992) 303–306.
[20] Sheetal, V.B. Taxak, Rajni Arora, Dayawati, S.P. Khatkar, Synthesis, structural and optical properties of $SrZrO_3$:Eu^{3+} phosphor, J. Rare Earths 32 (2014) 293–297.
[21] S.K. Gupta, A.K. Yadav, D. Bhattacharya, S.N. Jha, V. Natrajan, Visible light emitting Ln^{3+} ion (Ln = Sm, Eu and Dy) as a structural probe: a case study with $SrZrO_3$, J. Lumin. 164 (2015) 1–22.
[22] Y. Jin, Y. Hu, L. Chen, X. Wang, G. Ju, Z. Mou, Luminescence properties of dual-emission (UV/visible) long afterglow phosphor $SrZrO_3$:Pr^{3+}, J. Am. Ceram. Soc. 96 (2013) 3821-3227.
[23] J. Huang, L. Zhou, Z. Wang, Y. Lan, Z. Tong, F. Gong, J. Sun, L. Li, Photoluminescence properties of $SrZrO_3$:Eu^{3+} and $BaZrO_3$:Eu^{3+} phosphors with perovskite structure, J. Alloys Compd. 487 (2009) L5–L7.
[24] H. Zhang, X. Fu, S. Niu, Q. Xin, Synthesis and photoluminescence properties of Eu^{3+}-doped $AZrO_3$ (A = Ca, Sr, Ba) perovskite, J. Alloys Compd. 459 (2008) 103–106.
[25] H. Rétot, A. Bessière, A. Kahn-Harari, B. Viana, Synthesis and optical characterization of $SrHfO_3$:Ce and $SrZrO_3$:Ce nanoparticles, Opt. Mater. 30 (2008) 1109–1114.
[26] D. Hreniak, W. Strek, J. Amami, Y. Guyot, G. Boulon, C. Goutaudier, R. Pazik, The size-effect on luminescence properties of $BaTiO_3$:Eu^{3+} nanocrystallites prepared by the sol-gel method, J. Alloys Compd. 380 (2004) 348–351.
[27] H. Wang, N. Yoshikawa, S. Yoshikado, T. Aruga, Mutually pumped phase conjugator with a rainbow configuration in $BaTiO_3$:Ce crystal using nanosecond pulses, Opt. Lett. 21 (1996) 561–563.
[28] M. Dhanalakshmi, H. Nagabhushana, G.P. Darshan, R.B. Basavaraj, B. Daruka Prasad, Sonochemically assisted hollow/solid $BaTiO_3$:Dy^{3+} microspheres and their applications in effective detection of latent fingerprints and lip prints, J. Sci:Adv. Mater. Dev. 2 (2017) 22–33.
[29] H. Li, Y. Zhang, L. Shao, Z.M. Htwe, P. Yuan, Ratiometric temperature sensing based on non-thermal coupling levels in $BaZrO_3$:Yb^{3+}/Er^{3+} ceramics, Opt. Mater. Express 7 (2017) 3003–3010.
[30] H. Li, Y. Zhang, L. Shao, P. Yuan, X. Xia, Influence of pump power and doping concentration for optical temperature sensing based on $BaZrO_3$:Yb^{3+}/Ho^{3+} ceramics, J. Lumin. 192 (2017) 999–1003.
[31] S.K. Gupta, N. Pathak, R. Gupta, S.K. Thulasidas, V. Natarajan, Probing the oxidation state and coordination geometry of uranium ion in $SrZrO_3$ perovskite, J. Mol. Struct. 1068 (2014) 204–209.
[32] A. Ahtee, M. Ahtee, A. Glazer, A. Hewat, The structure of orthorhombic $SrZrO_3$ by neutron powder diffraction, Acta Crystallogr. B 32 (1976) 3243–3246.
[33] H. Fujimori, M. Kakihana, K. Ioku, S. Goto, M. Yoshimura, Structural phase transitions between 700 and 850 °C in $SrZrO_3$ studied by Raman spectroscopy, J. Chem. Soc. Jpn. 112 (4) (2004) 189–192.
[34] S. Amisi, E. Bousquet, K. Katcho, P. Ghosez, First-principles study of structural and vibrational properties of $SrZrO_3$, Phys. Rev. B Condens. Matter 85 (2012) 064112.
[35] F. Shi, K. Liang, Z.-M. Qi, Investigation of the crystal structure, lattice vibration and dielectric property of $SrZrO_3$ ceramic, J. Mater. Res. 31 (2016) 3249–3254.
[36] V. Singh, G. Sivaramaiah, J.L. Rao, S.H. Kim, Luminescence and electron paramagnetic resonance investigation on ultraviolet emitting Gd doped $MgAl_2O_4$ phosphors, J. Lumin. 143 (2013) 162–168.
[37] A. Endruweit, M.S. Johnson, A.C. Long, Curing of composite components by

ultraviolet radiation: a review, Polym. Compos. 27 (2006) 119–128.
[38] J.F. Quinn, L. Barner, C. Barner-Kowollik, E. Rizzardo, T.P. Davis, Reversible Addition−Fragmentation chain transfer polymerization initiated with ultraviolet radiation, Macromolecules 35 (2002) 7620–7627.
[39] W.H. Glaze, J.-W. Kang, D.H. Chapin, The chemistry of water treatment processes involving ozone, hydrogen peroxide and ultraviolet radiation, Ozone Sci. Eng. 9 (1987) 335–352.
[40] J. Nishii, N. Kitamura, H. Yamanaka, H. Hosono, H. Kawazoe, Ultraviolet-radiation-induced chemical reactions through one-and two-photon absorption processes in GeO_2–SiO_2 glasses, Optic Express 20 (1995) 1184–1186.
[41] S. Dogra, A.J. Kanwar, Narrow band UVB phototherapy in dermatology, Indian J. Dermatol. Venereol. Leprol. 70 (2004) 205–209.
[42] W. Köster, A. Wiskemann, Phototherapy with UV-B in vitiligo, Z. Hautkr. 65 (1990) 1022–1024.
[43] A.O. Chauhan, N.S. Bajaj, S.K. Omanwar, Synthesis and photoluminescence study of narrow-band UVB-emitting $LiSr_4(BO_3)_3:Gd^{3+}$, Pr^{3+} phosphor, Bull. Mater. Sci. 40 (2017) 1–6.
[44] A.O. Chauhan, A.B. Gawande, S.K. Omanwar, Narrow band UVB emitting phosphor $LaPO_4:Gd^{3+}$ for phototherapy lamp, Optik 127 (2016) 6647–6652.
[45] V. Singh, S. Borkotoky, A. Murali, J.L. Rao, T.K. Gundu Rao, S.J. Dhoble, Electron paramagnetic resonance and photoluminescence investigation on ultraviolet-emitting gadolinium-ion-doped $CaAl_{12}O_{19}$ phosphors, Spectrochm. Acta A 139 (2015) 1–6.
[46] M. Zahedi, S.A. Hassanzadeh-Tabrizi, A. Saffar-Teluri, Sol-gel synthesis and luminescence properties of $Ba_2SiO_4:Sm^{3+}$ nanostructured phosphors, Ceram. Int. 44 (2018) 10169–10174.
[47] Sk Khaja Hussain, J.S. Yu, Citrate-based sol-gel synthesis of blue- and green-emitting $BaLa_2WO_7:Tm^{3+}$ or Er^{3+} phosphors and their luminescence properties, Mater. Res. Bull. 95 (2017) 229–234.
[48] H. Kim, C. Yun, S. Wook Jeon, J. Key Lee, J. Pil Kim, Improved performance by plasma-treated silicate phosphor particles with a sol-gel derived protective coating of indium oxide, Opt. Mater. 53 (2016) 48–53.
[49] L. Zhang, J. Wang, D. Peng, F. Long, S. Mo, Y. Wu, Z. Zou, Photoluminescence and dielectric properties of pure/Yb-doped $SrZrO_3$ crystals, J. Phys. Chem. Solid. 104 (2017) 1–7.
[50] X. Li, W. Ma, J. Wen, Y. Bai, L. Sun, B. Chen, H. Dong, Y. Shuang, Preparation of $SrZrO_3$ thermal barrier coating by solution precursor plasma spray, J. Therm. Spray Technol. 26 (2017) 371–377.
[51] S. Wright, R.C. Barklie, Electron paramagnetic resonance characterization of defects in monoclinic HfO_2 and ZrO_2 powders, J. Appl. Phys. 106 (2009) 103917-15.
[52] M. Occhiuzzi, D. Cordischi, R. Dragone, Intrinsic and extrinsic paramagnetic centers in zirconia, J. Phys. Chem. 106 (2002) 12464–12469.
[53] J.-M. Costantini, F. Beuneu, S. Morrison-Smith, R. Devanathan, W.J. Weber, Paramagnetic defects in electron-irradiated yttria-stabilized zirconia: effect of yttria content, J. Appl. Phys. 110 (2011) 123506–123509.
[54] W.-C. Zheng, W. Fang, Y. Mai, Optical spectra and spin Hamiltonian parameters for rhombic Zr^{3+} in $Y_3Al_5O_{12}$, J. Appl. Phys. 101 (2007) 053911-053913.
[55] B. Boizot, G. Petite, D. Ghaleb, G. Calas, Radiation induced paramagnetic centres in nuclear glasses by EPR spectroscopy, Nucl. Instrum. Methods Phys. Res. B 141 (1998) 580–584.
[56] G.R. Asatryan, A.S. Kuzanyan, A.G. Petrosyan, A.K. Petrosyan, E.G. Sharoyan, Optical and EPR absorption spectra of yttrium aluminium garnet single crystals doped by Zr ions, Fiz. Tverd. Tela 27 (1985) 3441–3443.
[57] M.M. Abraham, L.A. Boatner, J.O. Ramey, M. Rappaz, The occurrence and stability of trivalent zirconium in orthophosphate single crystals, J. Chem. Phys. 81 (1984) 5362–5366.
[58] R. Cases, D.L. Griscom, D.C. Tran, Radiation effects in ZrF_4 based glasses: I. Electron spin resonance, J. Non-Cryst. Solids 72 (1985) 51–63.
[59] V. Ramaswamy, B. Tripathi, D. Srinivas, A.V. Ramaswamy, R. Cattaneo, R. Prins, Structure and redox behavior of zirconium in microporous Zr-Silicalites studied by EXAFS and ESR Techniques, J. Catal. 200 (2001) 250–258.
[60] C. Morterra, E. Giamello, L. Orio, M. Volante, Formation and reactivity of zirconium (3+) centers at the surface of vacuum-activated monoclinic zirconia, J. Phys. Chem. 94 (1990) 3111–3116.
[61] O.M. Orera, R.I. Merino, Y. Chen, R. Cases, P.J. Alonso, Intrinsic electron and hole defects in stabilized zirconia single crystals, Phys. Rev. B 42 (1990) 9782–9789.
[62] J.A.M. van Roosmalen, P. van Vlaanderen, E.H.P. Cordfunke, On the structure of $SrZrO_3$, J. Solid State Chem. 101 (1992) 59–65.
[63] M.M. Kuklja, Defects in yttrium aluminium perovskite and garnet crystals: atomistic study, J. Phys. Condens. Matter 12 (2000) 2953–2967.
[64] A.P. Patel, M.R. Levy, R.W. Grimes, R.M. Gaume, R.S. Frigelson, K.J. McClellan, C.R. Stanek, Mechanisms of nonstoichiometry in $Y_3Al_5O_{12}$, Appl. Phys. Lett. 93 (2008) 191902-191902-3.
[65] J. Dong, K. Lu, Noncubic symmetry in garnet structures studied using extended X-ray-absorption fine-structure spectra, Phys. Rev. B 43 (1991) 8808–8821.
[66] D. Truong, M.K. Devaraju, T. Tomai, I. Honma, Direct observation of antisite defects in $LiCoPO_4$ cathode materials by annular dark- and bright-field electron microscopy, ACS Appl. Mater. Interfaces 5 (2013) 9926–9932.
[67] N. Yuan, X. Liu, F. Meng, D. Zhou, First-principles study of La_2CoMnO_6: a promising cathode material for intermediate-temperature solid oxide fuel cells due to intrinsic Co-Mn cation disorder, J. Meng, Ionics 21 (2015) 1675–1681.
[68] R.D. Shannon, C.T. Prewitt, Effective ionic radii in oxides and fluorides, Acta Crystallogr. B 25 (1969) 925–946.
[69] Milan Mazur, Patrik Poprac, Marian Valko, Christopher J. Rhodes, 'U-spectrum' type of Gd(III) EPR spectra recorded at various stages of TEOS-based sol–gel process, J. Sol. Gel Sci. Technol. 79 (2016) 220–227.
[70] C.M. Brodbeck, L.E. Iton, The EPR spectra of Gd^{3+} and Eu^{2+} in glassy systems, J. Chem. Phys. 83 (1985) 4285–4299.
[71] R.D. Shannon, Revised effective ionic radii and systematic studies of interatomic distances in halides and chalcogenides, Acta Crystallogr. A32 (1976) 751–767.
[72] L. Jiansheng, L. Yanli, Effects of Sm^{3+} and Gd^{3+} Co-doping on thermo-physical properties of $LaMgAl_{11}O_{19}$, Trans. Indian Ceram. Soc. 73 (2014) 270–276.
[73] V. Singh, G. Sivaramaiah, J.L. Rao, R.S. Kumaran, P.K. Singh, T.-S. Kim, L.K. Kim, Luminescence and EPR studies of ultraviolet light emitting $La_2Zr_2O_7:Gd^{3+}$ phosphor powder, J. Mater. Sci. Mater. Electron. 26 (2015) 5195–5201.
[74] V. Singh, G. Sivaramaiah, J.L. Rao, S.H. Kim, Investigation of new UV-emitting, Gd-activated $Y_4Zr_3O_{12}$ phosphors prepared via combustion method, J. Lumin. 157 (2015) 82–87.
[75] S. Das, S. Som, C.Y. Yang, S. Chavhan, C.H. Lu, Structural evaluations and temperature dependent photoluminescence characterizations of Eu^{3+}-activated $SrZrO_3$ hollow spheres for luminescence thermometry applications, Sci. Rep. 6 (2016) 25787-1-13.